Fast, Triangular Voltage Clamp for Recording and Kinetic Analysis of an Ion Transporter Expressed in *Xenopus* Oocytes

Dietrich Gradmann* and Carl M. Boyd†
*Abteilung Biophysik der Pflanze der Universität, Untere Karspüle 2, 37073 Göttingen, Germany; and †Department of Oceanography, Dalhousie University, Halifax, Nova Scotia, B3H 4J1 Canada

ABSTRACT We present a procedure for determination of 11 system parameters of an ion transporter expressed in *Xenopus* oocytes. The experiments consist of fast triangular voltage-clamp experiments in the presence and absence of external substrate. A four-state enzymatic cycle operating between an external and an internal section of electrodiffusion is used for analysis. The explicit example treats experiments with the fungal $2H^+$-NO_3^- symporter EnNRT, a member of the major superfamily transporters. The results comprise a density of ≈150 fmol functional transporter molecules per oocyte, a gross charge number $z_E \approx -0.3$ of the empty binding site of the enzyme, individual rate constants for reorientation of the empty and occupied binding site in the range of 5–500 s^{-1}, electrical access sections between bulk solutions and reaction cycle of ~3% inside and 15% outside, an increase of internal NO_3^- at the plasma membrane from ~0.5 to ~2 mM during exposure to external NO_3^-, and $K_D \approx 0.3\ \mu M^3$ inside and $K_D \approx 3\ \mu M^3$ outside in binding the triplicate substrate ($2H^+ + NO_3^-$). The results compare well with the known structure of the lactose permease, another major superfamily transporter.

INTRODUCTION

The operation of enzymes comprises a catalytic reaction cycle of the active center and regulatory sites for appropriate modulation of the activity. In ion-translocating proteins, the corresponding mechanisms are called transport function and gating function, and are usually sensitive to the transmembrane voltage V. Three classes of ion transporters are distinguished: uniporters, cotransporters, and pumps.

Uniporters catalyze the transport of one charged substrate. By arbitrary distinction uniporters with a fast transport function (turnover $\geq 10^6\ s^{-1}$) are called channels and slow ones carriers. The gating functions of channels are electrophysiologically investigated in great detail using a consistent modeling approach of transitions between active (open) and inactive (closed) states (1,2) In contrast, the models for the transport function of channels vary between a series of energy barriers (3) and enzymatic cycles (4,5) depending on the actual observations. Very frequently, the shape of the steady-state IV curve of a uniporter cannot readily be assigned to a well-defined transport function. In these cases it is common to assume linearity or independent electrodiffusion for the sake of simplicity, even when the corresponding assumptions are in obvious disagreement with the experimental data.

In cotransporters the translocation of one substrate is coupled to the translocation of a second substrate. The turnover of cotransporters is much smaller than of channels and cannot be determined, therefore, by observations of individual protein molecules. Correspondingly, there are few studies on the electrical properties of cotransporters (6). Many cotransporters belong to the major facilitator superfamily (MSF) proteins that catalyze the transport of various substrates and are characterized by 12 membrane spanning domains. Amongst these proteins the H^+-lactose symporter from *Escherichia coli* has been investigated extremely well with respect to structure and function (7), but not electrophysiologically. On the other hand, the electrical properties of the $2H^+$-NO_3^- symporter EnNtr from the fungus *Emericella nidulans* (8) are known to the extent that a steady-state transport function and a gating function can be identified (9).

In pumps, ion translocation is coupled to a nontransport reaction of metabolic nature, e.g., ATP hydrolysis in case of the $Na^+/K+$-ATPase in animals and the H^+-ATPase in plants, or of nonmetabolic nature such as excitation by light, e.g., in case of bacteriorhodopsin (10).

Neither the transport function nor the gating function are known for light-driven pumps. In contrast, the steady-state transport function from several ATPases has been reported to be sigmoid, i.e., displaying a V-independent saturation current far from equilibrium (11–15). Non-steady-state kinetics of the pump transport function have been investigated by sinewave analysis for a plant pump (16) and by pulse relaxation analysis for the Na^+/K^+-ATPase (17). Also V-gating of pumps is known (14).

The aim of this overview about electrical properties of ion-translocating enzymes is to demonstrate the demand for a unifying concept to describe the transport functions. It is suggested that enzyme kinetics do provide such a concept, where the four-state model of Läuger (4) can be used as a basic formalism that may be simplified (11) or extended (18) depending on the experimental data available.

Here we present an example how the kinetics of an ion-translocating enzyme can be recorded and analyzed in

Submitted February 4, 2005, and accepted for publication April 14, 2005.

Address reprint requests to Dietrich Gradmann, Tel.: +49-551-39-7838; Fax: +49-551-39-7838; E-mail: dgradma@gwdg.de.

0006-3495/05/07/734/11 $2.00

doi: 10.1529/biophysj.105.060657

considerable detail by electrophysiological experimentation and corresponding enzyme kinetic analysis. We focused on the known $2H^+$-NO_3^- symporter EnNtr from *E. nidulans* (8), and used conventional equipment for studying electrical properties of ion-transporting enzymes expressed in *Xenopus* oocytes (19) as before (20,9). Less familiar may be the use of triangular *V*-protocols (9,14,21–23) used here again, and our presentation of enzyme kinetic relationships in current-voltage coordinates (9,21,22).

In voltage-clamp studies there are numerous time-varying driving functions (*V*-protocols) to record and analyze the temporal behavior of ion transporters. The most common ones are rectangular steps, ramps, sinewaves, and δ-pulses. The benefits and drawbacks of triangular *V*-protocols compared with those of more familiar functions are as follows.

The duration of rectangular steps is usually chosen to be long enough that all induced changes come to an apparent steady state. In case of investigating a large *V*-range, this may add up to long observation times and consequently more drift and/or fluctuations of the background. Furthermore, longer exposure to extreme voltages cause instabilities. In contrast, recordings of current-voltage-time relationships with triangular *V*-protocols are at least 10 times faster and require only short exposures to extreme *V*. However, the shorter observation time is traded in for less precision.

Ramps are frequently used when the observation time is short (24). With these records a wide *V*-range can be investigated within a short time but often at the expense of accuracy. Unfortunately, ramps are usually run only in one direction. So the temporal component in nonlinear responses cannot be identified unequivocally. If the ramps are run in the reverse direction as well—as in triangular waves—the time-variant component can be separated from the time-invariant one (many electrophysiologists call the time-variant difference between the results from the two ramp directions ''hysteresis''; in contrast, the original physical meaning of ''hysteresis'', for instance in magnetism, is a time-invariant residue after a temporal event).

Sinewaves of various frequencies provide the most accurate way to analyze complicated temporal relationships between the driving function and response in electrophysiology (25). However, this method requires linearity, i.e., the results are only valid if the response upon a sinewave is also a sinewave. And this condition does not apply for the whole *V*-range of electrophysiological interest. To use this powerful tool in nonlinear electrophysiology, one can apply large *V*-steps and superimpose small sinewaves (16). This approach is, however, much more time consuming again than a triangular *V*-sweep, which, in principle, comprises all the information as well, only with less precision and without all the analytical software available for technical purposes.

The use of δ-pulses (17) corresponds to the sinewave analysis with respect to the deep understanding of the theory and the requirement of linearity. Here, the response to one pulse comprises the whole spectrum of sinewaves, with the consequence again, that the benefit of shorter observation time is lost at the expense of accuracy (signal/noise ratio) compared to sinewave analysis. For this study, triangular *V*-clamp turned out to be appropriate. In principle, we recorded the non-steady-state electrical properties $I(V, t)$ of the heterologously expressed enzyme of interest in the kilohertz range within an unusually wide range of transmembrane voltage (V) between -200 and $+100$ mV, using *V*-clamp techniques with fast, triangular *V*-protocols, to overcome the steady-state instabilities of the oocyte membrane at large deflections from the resting *V*. The experimental results have been used to determine the parameters of a reaction kinetic model.

In a previous study (9) the results from slower (± 0.1 Vs^{-1}) triangular *V*-clamp on EnNtr in *Xenopus* oocytes have already been analyzed with a similar model. There are, however, two major differences between that previous study and this one:

First, in the previous approach two alternative model versions have been distinguished, one with an electroneutral binding site $z_E = 0$ and one with an electroneutral enzyme-substrate complex ($z_E = -z_S$, with z_S being the charge of the substrate); in contrast, for this study a gross charge number z_E is used, which may in principle assume any rational value, like apparent gating charges in Boltzmann equations or Hill coefficients in logistic functions. The impact of z_E on the shape of $I(V)$ relationships (exponential rising or falling) has already been pointed out in a theoretical note (23). Here, this concept of z_E is applied to experimental data the first time.

Second, in previous studies (9,22), steady-state kinetics, $I_a(V)$, have been assumed for the active enzymatic reaction cycle, and non-steady-state properties $I(V, t) = I_a(V)\, p_a(V, t)$ of the recordings have been assigned to the temporal kinetics $p_a(V, t)$ of the activity p_a of the enzyme (*V*-gating). This was appropriate as long as the *V*-protocol was slow compared to the enzymatic cycle. In contrast, for this study the *V*-protocol is much faster than *V*-gating ($p_a \approx const$), and the observed non-steady-state $I(V, t)$ can be assigned to the temporal characteristics of the active reaction cycle, $I_a(V, t)$ directly.

Ultimate understanding of the function of a protein requires a consistent model that quantitatively accounts for both, structural and kinetic details. For this investigation the crystal structure of EnNRT itself is not available. However, because this enzyme is a member of the MSF transporter that shares many structural properties, the kinetic information from EnNRT presented here can be discussed with respect to the structure of another MSF transporter, the lactose permease of *E. coli* that is known in great detail (7). This knowledge gave rise to a mechanistic model of the operation of MSF transporters on a qualitative level. It seems to hold not only for the translocation of lactose but also for alternate substrates such as glycerole-3-phosphate (26). Therefore, the numerical results presented here are considered to be relevant for MSF transporters in general. The corresponding discussion will focus on the lactose permease.

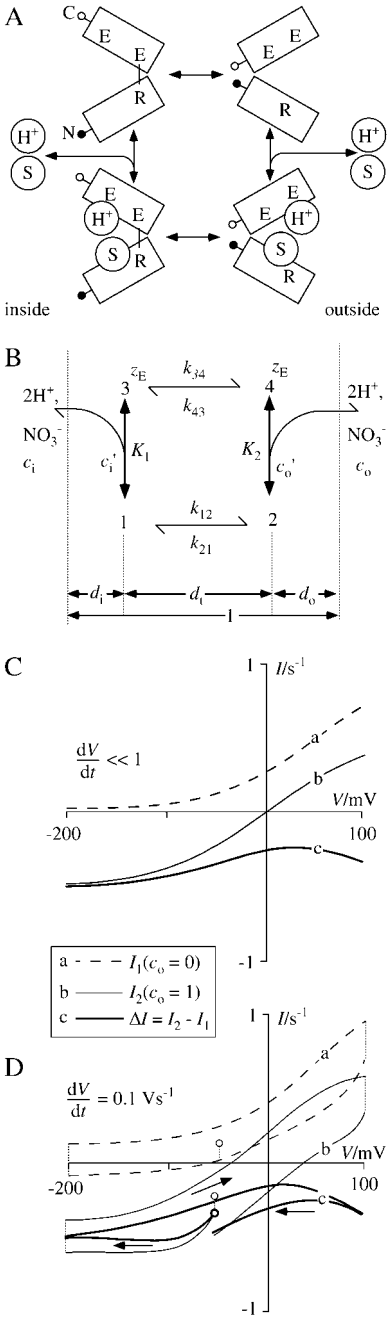

FIGURE 1 Model for analysis of $\Delta I(V, t)$ records of an ion-transporting enzyme in a membrane with background conductance, obtained from $I(V, t)$ relationships of the membrane in presence and absence of external substrate. (*A*) Simplified reaction scheme of the lactose transporter according to Abramson et al. (7); (*C* and *N*) C- and N-terminus of monomeric protein; one rectangle reflects half a monomer with six membrane-spanning domains each. (Outer and inner *E*) Glu^{269} and Glu^{325}, respectively; (*R*) Arg^{144}. (*B*) Reaction scheme of four-state enzymatic reaction cycle assuming fast binding/release equilibrium, and a gross charge z_E of empty binding site; kinetic partitioning of total electrical distance (1) in sections d_i, d_t, and d_o, of internal access section, enzymatic transport cycle, and external access section, respectively. (*C*) Steady-state $I(V)$ relationships of model (Eq. 4) with normalized currents (in s^{-1}) and simplistic parameter configuration for a uniporter for $z_S = 1$: $N_{tr} = 1$ (one transporter molecule), $z_E = 0$, d_i and $d_o = 0$ ($d_t = 1$), rate constants k^0_{12}, k^0_{21}, k^0_{34}, $k^0_{43} = 1\ s^{-1}$, $K_1 = 1\ mM^{-1}$, $c_i = 1$ mM. (*a*) In absence of external substrate; (*b*) in presence of 1 mM external substrate; currents $I_c = I_b - I_a$. (*D*) Non-steady-state $I(V, t)$ relationships upon triangular *V*-protocol with slopes of $\pm 0.1\ Vs^{-1}$, starting from holding voltage $V_0 = -50$ mV, passing $V_1 = -200$ mV, $V_2 = +100$ mV, and returning to V_0. Assumed normalized membrane capacity is $1\ V^{-1}$. Small circles mark beginning of record and arrows mark temporal direction; identification marks *a*, *b*, and *c* are the same as in panel *C*.

Fig. 1 *A* shows a simplified reaction cycle of this enzyme according to Fig. 6 in Abramson et al. (7). One simplification is lumping binding and release reactions of both substrates on each side into two equilibria, because these reactions are too fast to be resolved individually by electrophysiological experiments. This simplification reduces the employed number of states from six to four. The scheme in Fig. 1 *A* considers the functional monomer with 12 membrane spanning domains as a pair of a C-terminal and an N-terminal section, each represented by a rectangle comprising six membrane spanning domains. There is one binding site for the substrate S and the cosubstrate H^+ about in the middle of the protein that is also the approximate pivot point for antiparallel conformational changes of the two sections, causing the cavity between the two sections with the binding sites to be open either to the inside or to the outside. The number of critical amino acids has been reduced also to an inner E (Glu^{325}) and an outer E (Glu^{269}) in the C-section, and an R (Arg^{144}) in the N-section. As for the nitrate-H^+ symporter it would make immediate sense that NO_3^-, binds to the positive residue of an Arg, and H+ to the negative residue of Glu. During the conformational change of the loaded binding site from external to internal orientation H^+ changes its position from Glu^{269} to Glu^{325}, and a salt bridge is formed between Glu^{269} and Arg^{144} stabilizing the inward oriented conformation. These changes correspond to the transition between state 2 and state 1 in the formal reaction cycle of Fig. 1 *B*. Corresponding relationships between the physical model in Fig. 1 *A* and the kinetic model in Fig. 1 *B* are evident. They will be used in the Discussion for a physical interpretation of the numerical results. These comments are an attempt to interpret and combine structural data with electrophysiological data; they fulfill constraints from both approaches, but must be regarded as reasonable interpretations rather than confirmations.

MATERIALS AND METHODS

Cells and experimental procedures

Xenopus oocytes have been obtained and treated as described previously (9). To achieve good temporal resolution of the *V*-clamp experiments, low resistance (<0.5 MΩ) pipettes were used for current injection. The clamp currents were routinely low-pass filtered with 5 kHz by the four-pole Bessel filter of the measuring device (DAGAN TEV-200), digitized at 40 kHz, and sampled in intervals of typically 0.1–1 ms, depending on the slope of the triangular *V*- protocol.

Theoretical background

Performance and analysis of substrate-induced currents in *V*-clamp experiments with triangular *V*-protocols have already been reported in some detail (9,22,23). Nevertheless, some definitions and routines may be recalled explicitly:

Fig. 1 *B* shows a four-state reaction cycle of an ion-translocating enzyme (23) with one global binding site for the three substrate ions alternating its orientation toward inside or outside in occupied form (states 1 and 2) or empty (states 3 and 4). The four states have the occupancies p_1 to p_4 ($p_1 + p_2 + p_3 + p_4 = 1$). The empty states 3 and 4 have the gross charge number z_E, a rational number that reflects the charged residues in the vicinity of the empty binding site. The charge of the substrate is an integer number z_S that will be the sum $2z_{H+} + z_{NO3-} = 1$ in the present case of a $2H^+$-NO_3^- symporter. So the states 1 and 2 of the loaded complex will have the charge $z_C = z_E + 1$. One has to be aware that the transport cycle itself senses only a portion d_t of the entire transmembrane voltage V, and that the rest of the voltage drop, d_i and d_o, takes place in the corresponding inner and outer sections between bulk and binding sites (18,27). With this approach, the actual binding/release reactions (k_{31}/k_{13} inside, and k_{42}/k_{24} outside) can be assumed to sense only a negligible fraction of the transmembrane voltage (V). So the rate constants k_{12}, k_{21}, k_{34}, k_{43} for reorientation of the binding site along the electric field are *V*-sensitive in the form

$$k_{12} = k_{12}^0 \exp(z_C d_t u/2) \tag{1a}$$

$$k_{21} = k_{21}^0 \exp(-z_C d_t u/2) \tag{1b}$$

$$k_{34} = k_{34}^0 \exp(z_E d_t u/2) \tag{1c}$$

$$k_{43} = k_{43}^0 \exp(-z_E d_t u/2), \tag{1d}$$

where the superscript ^{0} marks the particular rate constant at $V = 0$, $u = VF/(RT)$ is the normalized transmembrane voltage with the usual thermodynamic meanings of F, R, and T, and the factor 1/2 in the exponents reflects symmetry of the Eyring barrier (for the necessity of this assumption, see Gradmann and Boyd (23)). Correspondingly, the electrical distances d_i and d_o of the inner and outer access section ($d_i + d_o = 1 - d_t$) affect the effective substrate concentrations c_i' and c_o' at the binding site inside and outside by

$$c_i' = c_i \exp(z d_i u) \tag{2a}$$

$$c_o' = c_o \exp(-z d_o u), \tag{2b}$$

where c_i and c_o are the inner and outer bulk concentration. The distinction between c and c' has to be made for the two substrates H^+ and NO_3^- separately because of their different z ($z_H = +1$, $z_{NO3} = -1$). So, the ratio c'/c for H^+ will be the inverse of c'/c for NO_3^-.

Binding and release of substrate are assumed to be fast reactions (k_{31}, k_{13}, k_{42}, $k_{24} \gg k_{12}$, k_{21}, k_{34}, k_{43}) in *V*-independent equilibrium, which can be summarized by the stability constants (Fig. 1 *B*):

$$K_1 = K_1^0 c_i' = k_{31}^0 \times c_i'/k_{13} \tag{3a}$$

$$K_2 = K_2^0 c_o' = k_{42}^0 \times c_o'/k_{24}, \tag{3b}$$

where the superscript ^{0} marks reference conditions (all $c' = 1$ mM) again. Because microscopic reversibility dictates

$$K_2^0 = K_1^0 k_{12}^0 k_{43}^0/(k_{21}^0 k_{34}^0), \tag{3c}$$

the reaction cycle is determined by five independent kinetic parameters (we chose k_{12}^0, k_{21}^0, k_{34}^0, k_{43}^0, and K_1^0) under reference conditions (1 mM substrate concentrations and $V = 0$ mV).

The steady-state $I(V)$ current-voltage relationships of N_{tr} mol transporters at different substrate concentrations c_i, c_o, can be derived as

$$I(V, c_i, c_o) = z_S F N_{tr} \frac{K_1 k_{12} k_{43} - K_2 k_{21} k_{34}}{K_1 K_2 (k_{12} + k_{21}) + K_1 (k_{12} + k_{43}) + K_2 (k_{21} + k_{34}) + k_{34} + k_{43}}, \tag{4}$$

where V enters Eq. 4 via u by Eqs. 1 and 2, and c_i, c_o by Eqs. 2 and 3.

Fig. 1 *C* shows (normalized by setting the scaling factors $z_S F N = 1$) two $I(V)$ curves of the model with a very simple parameter configuration, in the absence (*a*) and presence (*b*) of external nitrate. Due to background currents, these records are usually not available as such. The difference curve $c = \Delta I(V)$, however, is frequently the available information, when experimental $I(V)$ relationships including background currents are recorded from a biological membrane in the presence and absence of external substrate.

As mentioned in the Introduction, in these experimental systems, non-steady-state properties $I(V, t) = I_a(V) p_a(V, t)$ with *V*-protocols slower than ± 1 Vs^{-1} can be assigned to *V*-gating (9). With *V*-protocols of ± 1 Vs^{-1} and faster, however, the gating effects vanish ($p_a \approx const$), and the temporal feature $I_a(V, t)$ of the active reaction cycle itself becomes more and more evident. This feature behaves electrically as an extra capacitance with a conductance in series, where the capacitance reflects a pool of mobile charges (certain states of a transporter) in the membrane, and the serial conductance corresponds to the mobility of these states in reorientation upon changes of the electric field (16,28). Here we omit this intermediate formalism of linear circuitry and describe the observed records directly with the non-steady-state behavior $I_a(V, t)$ of the active reaction cycle.

For experimental control and calculations of the temporal behavior, the apparent ramps have actually been performed by a series of short ($\Delta t \leq 1$ ms) and small ($\Delta V = \pm 1$ mV) *V*-steps. Current records were calculated iteratively, starting from a steady-state current I_0 at the holding V and adding subsequent current increments

$$\Delta I_i(\Delta t) = (I(V_i) - I_{i-1}) \exp(-\Delta t/\tau), \tag{5}$$

which result from the difference between the steady-state current $I(V_i)$ for the actual V and the preceding value I_{i-1} of the actual current, the temporal increment Δt of, e.g., 0.2 ms, and the time constant

$$\tau = 1/(k_{12} + k_{21} + k_{34} + k_{43}), \tag{6}$$

at the actual V (Eqs. 1a–1d). Equations 5 and 6 are used to describe the temporal behavior of the reaction cycle.

Corresponding model calculations are shown in Fig. 1 *D*, with the same system parameters and scenarios as in Fig. 1 *C*, only with much faster $\Delta V/\Delta t$; so the capacitive currents (*vertical dashed traces*) in the $I(V, t)$ records become evident, and—most important here—the bold $\Delta I(V, t)$ record, *c*, reveals (after automatic elimination of all background features, in particular of the membrane capacitance) the vertical separation of the two $\Delta I(V, t)$ branches, recorded with positive or negative $\Delta V/\Delta t$ ramps.

Fits have been carried out using a ''direct search'' algorithm (29) with common, small increments for all parameters, which turned out to be slow but more successful than faster gradient methods (even Simplex) in avoiding convergence to side minima, provided the start increment is small enough. The programs for data analysis are written in Turbo-Pacal and are available on request.

RESULTS AND DISCUSSION

Individual, fast $\Delta I(V, t)$ records

Fig. 2 shows the records of a typical voltage-clamp experiment for determination of the turnover of EnNtr, functionally expressed in a *Xenopus* oocyte. The two top panels *A* and *B* show the original time courses of the recorded V (*A*), which follows the command voltage closely, and of the clamp currents (*B*) in absence (*A*) and presence (*B*) of 60 μM NO_3^-

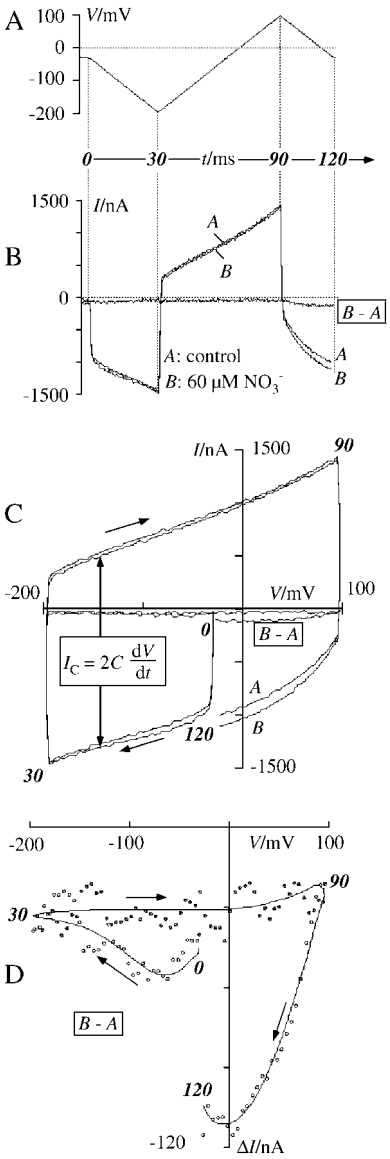

FIGURE 2 Typical EnNtr-mediated, $[NO_3^-]_o$-induced $\Delta I(V, t)$ in *Xenopus* oocytes, recorded with fast (here ± 5 Vs^{-1}), triangular V-protocol; bold, italic numbers in every panel mark times (in ms) after start of triangular V-protocol. (*A*) Time course of recorded V. (*B*) Current response of oocyte membrane in absence (*A*) and presence (*B*) of 60 μM external NO_3^-, dominated by RC properties of oocyte membrane; $B - A$: remaining difference, $\Delta I(V, t)$, after eliminating mutual current components in *A* and *B* by subtraction. (*C*) Same data as in Fig. 2, *A* and *B*, replotted in $I(V)$ coordinates, enabling easy reading of capacity, and revealing basic kinetics of $B - A = \Delta I(V, t)$. (*D*) Upscaling of $\Delta I(V, t)$ experimental data (points, moving averages from five samples) from Fig. 2 *C* and fit (*curve*) by model in Fig. 1.

in the external medium. The prevailing currents in Fig. 2 *B* are due to the background admittance of the oocyte membrane, with more or less linear slopes, and almost vertical offsets $I_C = C(\Delta V/\Delta t)$ due to the membrane capacitance. In forming the difference $B - A$, the background electrical properties of the oocyte membrane cancel out, and the small difference current, $B - A$, comprises the EnNtr-mediated, nitrate-induced $\Delta I(V, t)$. Compared with the individual curves *A* and *B*, the differences $B - A$ are small and more noisy, of course; but the scatter is always smaller than the differences.

Capacitance

The very data of Fig. 2, *A* and *B*, are replotted in current/voltage coordinates in Fig. 2 *C*, which allows a convenient reading of the oocyte capacitance $C = I_C/(2|\Delta V/\Delta t|) \approx (1700$ nA$)/(10$ $Vs^{-1}) = 170$ nF in this case of a $\Delta V/\Delta t$ change from -5 Vs^{-1} to $+5$ Vs^{-1} (see also Schmitt and Koepsell (30)). The capacitance indicates a membrane area of $\sim$17 or 34 mm^2, depending on whether for the membrane capacitance a traditional value of 10 mFm^{-2} is assumed or an updated one of ~ 5 mFm^{-2} (31).

Measuring ranges

According to common electrophysiological experience, steady-state $I(V)$ from *Xenopus* oocytes could be reproduced well within a range from ~ -150 to $+50$ mV. This V-range has also been explored for studying the temporal characteristics of V-gating of EnNtr using triangular V-protocols with slopes of ± 0.1 Vs^{-1} (9). When using steeper slopes, the V-gating phenomena disappeared at $\sim \pm 1.0$ Vs^{-1}, resulting in virtual coincidence of the $I(V, t)$ relationships when recorded with positive or with negative slopes of the command V. Exploring these apparent steady-state $I(V)$ relationships, we noticed still good reproducibility when the V-range was extended to -200 and $+100$ mV, where genuine steady-state recordings are usually no longer stable.

Using even steeper slopes up to ± 10 Vs^{-1} revealed the non-steady-state phenomena, which are the main subject of this study. In an initial approach, these phenomena were investigated in the conservative V-range from -120 to $+50$ mV. Because the kinetic analysis based exclusively on these experiments showed some ambiguities, which are not further discussed here, the wide V-range from -200 to $+100$ mV was routinely used for the main series of the experiments presented here.

Preliminary recordings with even steeper slopes of ± 20 Vs^{-1} seemed to be biased by artifacts, immediately after the changes of sign in $\Delta V/\Delta t$. So, the dynamic range from ± 2 to ± 10 Vs^{-1} explored here was limited at the lower end by the apparent steady-state characteristics at 1 Vs^{-1}, and at the upper end by the present performance of the apparatus.

Fitting the model to the experimental data

Fits have been carried out to individual records such as in Fig. 2 *B*, or to average data as shown in each panel of Fig. 3. The most critical approach is a simultaneous fit of the model with a common set of parameters to data sets from several experimental conditions. Such a fit is given in the box in Fig.

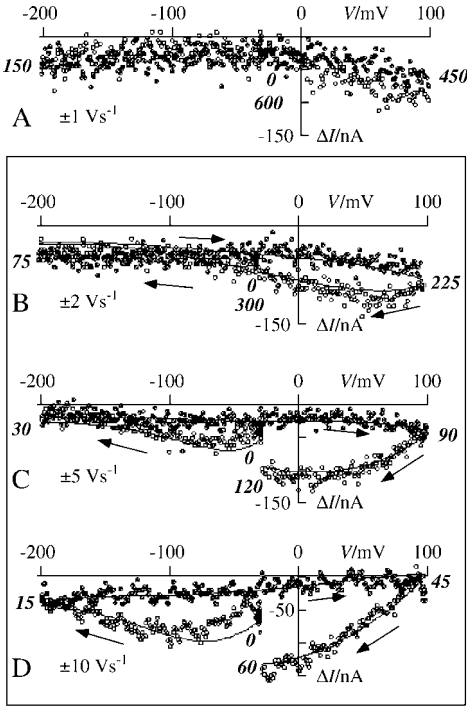

FIGURE 3 Average data of $n = 8$ $\Delta I(V, t)$ records as in Fig. 2 *D* from one oocyte (*a*) recorded with different speed $\Delta V/\Delta t$ of triangular *V*-protocol as marked in $\pm$Vs^{-1}. (*Solid* and *open symbols*) Data from positive and negative *V*-slope, respectively. (*A*) Quasi-steady-state, virtual coincidence of data from positive and negative slope, not fitted. (Boxed *B–D*) Fitted by model in Fig. 1 *B* with one common set of parameters as listed for cell *a* in Table 1.

3, where the data from three different triangular speeds are described by the model with the very same parameters.

The difference of currents between the beginning and end of a record is due to the start from steady-state conditions. This difference would disappear under continuous periodic cycles (22).

Depending on the start parameters, the fit increments, and the duration of the fits, there is some variability of the numerical results, of course, even when visual inspections of the fits are equally satisfying, i.e., when the numerical improvements in the sum of the square differences are significant but small. The data in Table 1 from three independent cells (*a*, *b*, *c*) and two different increments (10^{-3} for *a*, *b*, *c* and 10^{-4} for *a′*, *b′*, *c′*) convey a realistic impression. Initially, k^0_{34} and K^0_1 were fitted individually (*a*, *b*, *c*) until their antiparallel impact became obvious. So the subsequent fits (*a′*, *b′*, *c′*) were performed with K^0_1 fixed at an arbitrary value of 10 μM^{-3}. Because the results of *a* and *b* from data over the full *V*-range from -200 to $+100$ mV turned out to be very similar, they have been assumed to be representative, and the rounded results of *a* were used as reference ''Refer'' for further tests.

Solution *c* shows a more negative z_E and smaller d_o than in solutions *a* and *b*. This may indicate the position of a negative charge in the outer access section. This conjunction may be accounted for in fit *c* by integration of this charge and the external access section into the apparent parameters z_E and d_t.

Underlaying *I*(*V*) and *I*(*V*, *t*)

The performed fits of the model to the $\Delta I(V, t)$ records comprise calculations of the $I(V, t)$ relationships in absence and presence of external substrate, which can be understood more easily than the resulting $\Delta I(V, t)$ records. For the parameter configuration ''Refer'' in Table 2, Fig. 4 shows these parent relationships for steady-state (Fig. 4 *A*) and for non-steady-state conditions as under triangular *V*-clamp with slopes of ± 5 Vs^{-1} (Fig. 4 *B*). These two graphs correspond to the schematic Fig. 1, *C* and *D*, (without capacitive currents) in the ''Theoretical background'' section above.

Fig. 4 *A* shows the reconstructed steady-state currents of the transporter (Eq. 4 with parameters in Table 3) in absence (*a*) and presence (*b*) of external substrate with a typical reversal of the sign at thermodynamic equilibrium in case *b*, here at $E_{Sy} \approx +20$ mV. These reconstructed curves, which are normally not recognized within the background currents, can be interpreted in a straightforward way. Curve *a* indicates substantial outward currents in the absence of external substrate, i.e., loss of substrate NO_3^- (and H^+) under control conditions, which is usually not recognized within the ''background'' currents. These plots reflect the experimental situation occurring when repetitive exposures to external substrate cause substantial substrate concentrations in the vicinity of the membrane inside, which do not entirely vanish during the short periods of starvation.

TABLE 1 Fit analysis results from individual oocytes

Parameter/unit	N_{tr}/fmol	z_E	d_i/%	d_o/%	k^0_{12}/s^{-1}	k^0_{21}/s^{-1}	k^0_{34}/s^{-1}	k^0_{43}/s^{-1}	$K^0_1/(\mu M)^{-3}$	c_{i0}/μM	c_{i1}/μM
Start	100	0	10	10	10	100	100	100	10	1000	1000
a	150	−0.29	3	14	6.0	102	26	20	6.6	840	2530
a′	45	−0.43	1	18	23	580	74	39	10	1940	2290
b	120	−0.29	3	12	7.5	78	25	20	6.2	930	1590
b′	133	−0.40	0	18	9	540	3.8	18	10	80	120
c	510	−0.50	5	2	1.6	78	12	5	41	230	1850
c′	210	−0.38	22	1	4	390	11	16	10	450	4600

Parameter values found by fitting model in Fig. 1 *B* to average experimental data (*a*, $n = 8$, $C = 170$ nF; *b*, $n = 8$, $C = 167$ nF; *c*, $n = 4$, $C = 180$ nF); fit increments are: *a*, *b*, *c*, 10^{-3}; *a′*, *b′*, *c′*, 10^{-4}; *V*-range, cells *a* and *b* from -200 to $+100$ mV, cell *c* from -120 to $+50$ mV.

TABLE 2 Fit analysis for refit *a*

Parameter/unit	N_{tr}/fmol	z_E	d_i/%	d_o/%	k^0_{12}/s^{-1}	k^0_{21}/s^{-1}	k^0_{34}/s^{-1}	k^0_{43}/s^{-1}	$K^0_1/(\mu M)^{-3}$	$c_{i0}/\mu M$	$c_{i1}/\mu M$
Start	75	+0.20	1.5	7	3.0	200	12.5	40	7	400	5000
Refer	150	−0.30	3.0	14	6.0	100	25	20	7	800	2500
Found	172	−0.29	2.1	14	5.2	98	26	24	7	620	2750

Refit reference solution *a* from Table 1 with rounded parameters (Refer), using start parameters in row marked ''Start'', differing by factor 2 or 0.5 from reference values in row marked ''Refer''; K_1 fixed; start increment 10^{-5}, stop after 480 min with increment 10^{-6}; fitted values in row marked ''Found'' agree well with the values of the reference solution in row ''Refer''.

In initial experiments (not illustrated), we were impressed by the up to fivefold larger current responses ΔI_0 of NO_3^- starved cells at a fixed holding V (e.g., −40 mV), when they were exposed the first time to external NO_3^-, compared with the series of reproducible responses ΔI_n upon repetitive exposures that are systematically analyzed here. However, we were simultaneously puzzled by the finding that the resulting $\Delta I_0(V)$ curves did cross the V axis, which is considered to be thermodynamically ''forbidden'' for straightforward systems. In an earlier attempt (not published) we assigned this forbidden behavior to the operation of a second, allosteric (external) NO_3^- binding site, which has to be occupied for the transporter to be active. In accord with our previous conclusions about transinhibition (9) the present analysis shows, however, that such an additional activation site does not have to be assumed. This can be explained by Fig.4 *A*. If the internal NO_3^- concentration in the vicinity of the transporter is close to zero (before repetitive exposures), the control current *a* without charge supply would be zero at all V; and during exposure to external NO_3^-, the internal NO_3^- concentration (next to the membrane) rises substantially before the subsequent measurements are carried out in a quasisteady state. In this situation, when both external and internal $[NO_3^-]$ have changed from 0 to $\gg 0$, the $\Delta I(V)$ and $I(V)$ curves are identical and will cross the V axis at the equilibrium voltage of the transporter. In other words, the statement ''$\Delta I(V)$ curves induced by a change in external substrate don't cross the V axis'' holds only for constant internal substrate. In reality, however, (local and temporal) changes of internal substrate concentrations may be substantial; and these changes are also subject to the analysis presented herein (last two columns in Table 1).

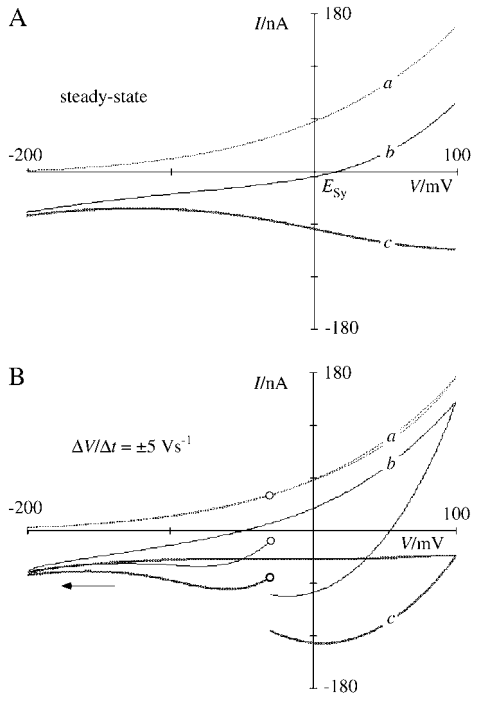

FIGURE 4 Reconstructed, electrodynamic properties of EnNtr, calculated by model in Fig. 1 with parameter set *a* in Table 2. Scenarios *a*, *b*, and *c* are the same as in Fig. 1, *B* and *C*. (*a*) No external NO_3^-; (*b*) with 60 μM external NO_3^-; (*c*) current differences *b* − *a*; steady-state ($|\Delta V/\Delta t| \ll 1$ Vs^{-1}). (*A*) Steady-state. (*B*) Non-steady-state example ($\Delta V/\Delta t = \pm 5$ Vs^{-1}).

In fitting the model to the experimental data upon repetitive exposures it turned out that k^0_{34} and K^0_1 cannot be well determined simultaneously because of complementary effects. This $k^0_{34} - K^0_1$ ambiguity at certain parameter configurations has been pointed out before (22). It can be solved, however, by the prime responses ΔI_0 ($\Delta I_0/\Delta I_n = 2.8 \pm 0.3$ SE, $n = 5$). With the notion of virtual absence of internal NO_3^-, K_1 vanishes, and with large K_2—the applied external $[NO_3^-]$ of 60 μM is three times higher than $K_M \approx 20$ μM (9,20)—Eq. 4 degenerates to $\Delta I_0 = z_S N_{tr} F k_{34} k_{21}/(k_{34} + k_{21})$. With $\Delta I_n \approx -60$ nA at the holding voltage $V_h \approx -30$ mV (Fig. 4 *A* (*c*)) and $\Delta I_0/\Delta I_n \approx 3$, ΔI_0 is ~−180 nA. So $k_{34} \approx 14.3$ s^{-1} at V_h can be isolated from the degenerated Eq. 4 with $k_{21} = k^0_{21}\exp(z_C d_t u/2) \approx 75$ s^{-1} at V_h ($z_S = 1$, $F \approx 10^5$ Asmol^{-1}, Table 2, Refer, gives $k^0_{21} \approx 100\,s^{-1}$, $z_C \approx 0.7$, $d_t \approx 0.8$, $N_{tr} \approx 150$ fmol). This $k_{34} \approx 14.3\ s^{-1}$ at V_h and Eq. 1c yields the desired $k^0_{34} \approx 13\,s^{-1}$ and consequently $K^0_1 \approx 3.5$ μM^{-3} ($K_{D1} = 1/K^0_1 \approx 0.3\,\mu M^3$) as well as $K^0_2 \approx 0.35$ μM^{-3} by Eq. 3c ($K_{D2} = 1/K^0_2 \approx 3\,\mu M^3$). In conclusion, all system parameters can be identified. The corresponding, complete numerical solution with revised values for k^0_{34} and K^0_1 is listed in Table 3. It allows the determination of an asymmetry ratio $r_{as} = k_{21}k^0_{43}/(k^0_{12}k^0_{34}) \approx 25$, which indicates that in the absence of a driving force, the binding site of the transporter is preferentially oriented toward the interior side of the membrane.

The $I(V)$ curve *b* in Fig. 4 *A* shows exponential increases of currents with large V-deflections from equilibrium at both ends—steeper in the positive V-range than in the negative

TABLE 3 Final fit analysis

Parameter/unit	N_{tr}/fmol	z_E	d_i/%	d_o/%	k^0_{12}/s^{-1}	k^0_{21}/s^{-1}	k^0_{34}/s^{-1}	k^0_{43}/s^{-1}	$K>^0_1/(\mu M)^{-3}$	$c_{i0}/\mu M$	$c_{i1}/\mu M$
	150	−0.3	3	14	6	100	13	20	3.5	800	2500

Revised parameter set from Table 1 *a* after elimination of k_{34}-K_1 ambiguity.

one. These exponential characteristics are numerically reflected by $-1 < z_E < 0$ (more detailed discussion of z_E below).

Fig. 4 *B* shows the dynamic features of the modeled transporter. Interestingly, the dynamic features are virtually absent in the control record *a* (absence of external substrate). This can be explained by focusing on state 2 in the model Fig. 1 *B*, Eq. 6, and the large values of k_{21} in Table 1. In the absence of external substrate, state 2 will be depleted (occupancy $p_2 = 0$); and k_{21} as by far the biggest of the four rate constants, has the strongest impact on τ. Because k_{21} affects the currents in form of the rate p_2k_{21}, its impact will be irrelevant at $p_2 = 0$. So in the absence of external substrate, $\tau = 1/(k_{12} + k_{21} + k_{34} + k_{43})$ will degenerate to a much larger $\tau_0 = 1/(k_{12} + k_{34} + k_{43})$, and the system becomes too slow to respond noticeably to the rapid *V*-protocol.

Noting $\tau \approx 1/k_{21}$, and $k_{21} \approx 100e^{-0.28u}$ (Eq. 1 Table 2, Refer), the current relaxation in the negative *V*-range is expected to be faster than in the positive *V*-range; this feature is reflected by the observation that the separation of the $\Delta I(V, t)$ between positive and negative $\Delta V/\Delta t$ slopes becomes evident in the negative *V*-range only at steeper $\Delta V/\Delta t$ slopes than in the positive *V*-range (Fig. 3). Correspondingly, in Fig. 5 *F* the continuous trace representing doubled k_{21} shows much less separation (faster relaxation toward steady state) of the two branches at the left $\Delta V/\Delta t$ reversal compared to the right one.

So, for the more obvious temporal effects in the positive *V*-range, a prominent role of k_{21} might also be expected, which turns out to be not true (compare Fig. 5, *E* and *F*). It is not k_{21} but k_{12} that effectively increases the strong separation of the two branches at the right $\Delta V/\Delta$ reversal (see Fig. 5, *E* and *F*) via an increase of the occupancy p_2. This increase of p_2 (and p_4) at positive *V* is a consequence of $z_E = -0.3$ and a correspondingly $z_C = +0.7$, which leads to a stronger accumulation of p_2 and p_4 via k_{12}/k_{21} than their depletion via k_{43}/k_{34}.

Test for ambiguities by refitting

Because of the limited accuracy due to the scatter of experimental data, multiparameter fits suffer from the problem whether a found solution is unique or a random member of a family of solutions. In this context, the antiparallel effects of k^0_{34} and K^0_1 (9) have already been pointed out and will be treated below again (e.g., Fig. 5 *J*). To search for still undiscovered and maybe more complicated relationships of this kind, the solution to be tested has been refitted with start parameters, which differed by factor 2 or 0.5 from the reference solution. The results for the paradigm *A* are listed in Table 2, and show good agreement between the fitted solution and the reference set ''Refer'' after a finite time of calculations when all parameters appeared to converge toward the reference values. This agreement excludes intrinsic ambiguities of the model due to undiscovered relationships between several parameters. It may be superfluous to state that unsuitable start parameters may lead to different ''solutions'' of the (re-) fits, which can be rejected, however, on the basis of larger σ values and/or diverging parameter values.

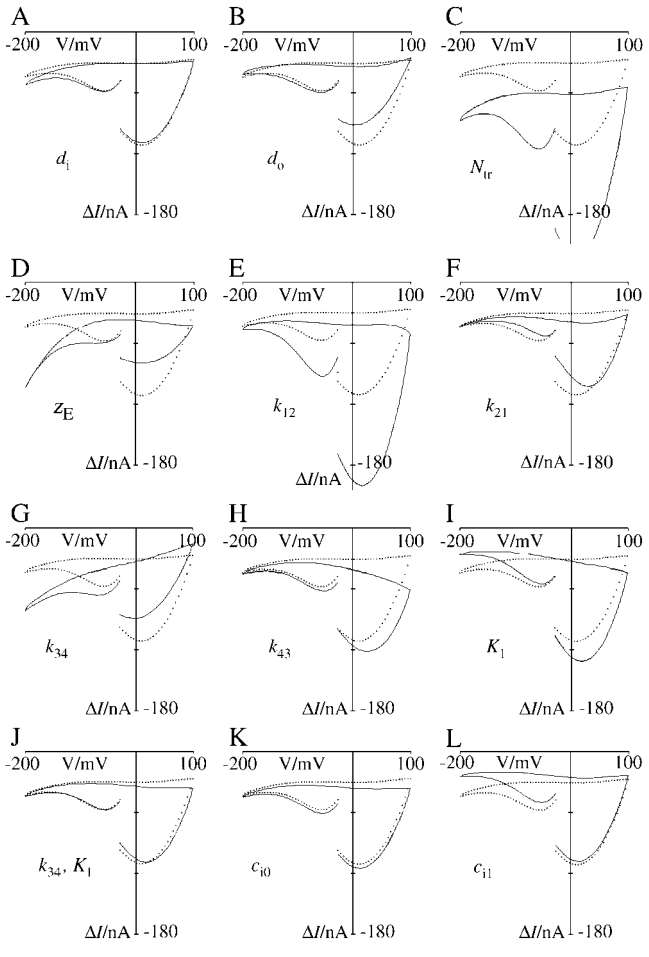

FIGURE 5 Impact of individual model parameters on shape of $\Delta I(V, t)$ records; definitions in Fig. 1 *B*; calculations with ± 5 Vs^{-1} slopes of *V*-protocol. The dotted lines give the reference calculated from the parameters in Table 2, row ''Refer''. The Refer curves are identical in each panel. The continuous line shows curves calculated with the same values except the one that is indicated in the panel. This parameter is doubled with respect to Refer.

Sensitivity analysis

Table 4 shows a numerical listing of the relative impact of the individual parameters on the shape of the found $\Delta I(V, t)$ function, normalized to the simple scaling effect of the density N_{tr} (100%). This listing shows that at the present parameter configuration, a percentage change in k^0_{12}, for instance, has a large impact on the shape, whereas, e.g., a change in d_i has little effect, which is not surprising in this particular case, because the absolute d_i is already nearly negligible. Furthermore, the similar entries (35) for k^0_{34} and K^0_1 in this table may appear coincidental or could indicate parallel as well as antiparallel effects of these two parameters on the shape of the $\Delta I(V, t)$. The graphical presentation (Fig. 5) of the specific effects of the individual parameters on the shape of $\Delta I(V, t)$ allows a much more detailed perception of the relationships. For example, the effects of doubling of k_{34} (Fig. 5 *G*) and of K_1 (Fig. 5 *I*) can roughly be seen as a counterclockwise (k_{34}) and clockwise (K_1) rotation about a common pivot point ($\sim$0 mV and -60 nA) by about the same angle, which causes compensation to virtual annihilation in case of a common change by the same factor (Fig. 5 *J*).

Physical interpretation

N_{tr}

The numerical value of $N_{tr} \approx 150$ fmol and the capacitance $C \approx 170$ nF can be used to estimate the density $D = N_{tr}/A$ of N_{tr} functionally expressed transporters per area A of plasma membrane of the oocyte. Using a conservative figure of the specific capacitance $c_m = 10$ mFm^{-2} of biomembranes, the determined capacity C of $\sim$170 nF (Fig. 2) can be used to estimate the membrane area of the tested oocyte as $A = C/c_m = 17 \times 10^{-6}$ m^2. So the density $D = N_{tr}/A$ will be 150 fmol/17×10^{-6} m^2 $\approx 10^{-8}$ mol m^{-2} or $\sim$0.6 transporters per membrane area unit of (10 nm)^2 with the Avogadro number $N_A \approx 6 \times 10^{23}$ molecules per mol. Using a more recent value of $c_m \approx 5$ mFm^{-2} (31) would yield a smaller density of $\sim$0.3 functional transporters per (10 nm)^2 membrane surface or $\sim$3000 transporters per μm^2. Similar densities of heterologously expressed membrane proteins in *Xenopus* oocytes have been reported (32), which confirms the validity of our approach.

z_E

The gross charge number $z_E \approx -0.3$ of the empty binding site (states 3 and 4 in Fig. 1 *B*) assigns a gross charge number $z_C \approx +0.7$ to the loaded states 1 and 2 in Fig. 1 *B*. As shown previously (22) this opposite sign introduces an opposite V-dependence of the reorientation of the charged and of the uncharged states. The consequence is that at increasing voltages of either sign the reaction cycle becomes exponentially faster by simultaneous increase of the reorientation speed of the empty state in one direction (e.g., inside to outside) and of the loaded state in the opposite direction (correspondingly outside to inside). This will result in an exponential increase of the current, $I/I_{ref} \approx \exp(0.3u)$, for large voltage deviations, limited in steepness by the smaller amount (0.3) of the two corresponding charges ($0.3 = |z_E = -0.3| < 0.7 = |z_C = +0.7|$) in our case. The corresponding shape of the steady state $I(V)$ of the transporter (Fig. 4 *A* (*b*)) has already been pointed out, as well as the impact of z_E and z_C on the temporal characteristics (Fig. 4 *B*) via the V-dependent distribution of the four occupancies.

The structural equivalent of $z_E \approx -0.3$ is some predominance of negative residues of the unoccupied binding site, which corresponds to the simplified model in Fig. 1 *A*.

d_i, d_o

The apparent access distances d_i and d_o may reflect pore sections. As mentioned above, these distances and z_E may be affected simultaneously, depending on the location of the hypothetical border between access distance and reaction cycle. The same relationship between z_E and access distances can explain the discrepancy of $d_i < d_o \approx 10\%$ found here and $d_o < d_i \approx 50\%$ reported previously for the same enzyme (9), because $z_E = 0$ was assumed in this previous study, whereas $z_E \approx -0.3$ is determined here.

In comparison to ion channels with rapid turnover ($\geq 10^6$ s^{-1}) of the selectivity filter (33,34), the present finding of small d_i, d_o is consistent with the slower turnover ($<10^3$ s^{-1}) of the symporter under investigation, which amounts to a larger voltage drop (electric distance) across the reaction cycle compared to the access sections, because the electrical access distances d_i, d_o are relative parameters with respect to the voltage drop d_{tr} across the enzymatic transport cycle ($d_i + d_{tr} + d_o = 1$).

With respect to the structure of MSF transporters, $d_i < d_o$ seems to reflect better electrical contact between the binding site and the inner solution than with the outer one. This is consistent with the structural notion that MSF transporters are preferentially open to the inner side (7). This property is also reflected by the ratio $k^0_{21}k^0_{43}/(k^0_{12}k^0_{34}) \approx 25$ (Table 3), which points to a strong preference of opening toward the internal side.

TABLE 4 Sensitivity analysis by percentage

Parameter/unit	N_{tr}/fmol	z_E	d_i/%	d_o/%	k^0_{12}/s^{-1}	k^0_{21}/s^{-1}	k^0_{34}/s^{-1}	k^0_{43}/s^{-1}	$K^0_1/(\mu M)^{-3}$	c_{i0}/μM	c_{i1}/μM
	100	35	4	16	80	19	35	38	35	13	28

Numerical sensitivity analysis of solution *a*. Relative impact, 100 σ_i/σ_{Ntr}, of small (10%) change of individual parameter i on deviation σ_i from reference solution, compared to reference deviation σ_{Ntr} (proportionality). For details see graphic analysis in Fig. 5.

k_{ij}

Referring to the final parameter set in Table 3 and to Eq. 1, the four V-sensitive rate constants amount to $k_{12} \approx 6e^{0.28u}$ s^{-1}, $k_{21} \approx 100e^{-0.28u}$ s^{-1}, $k_{34} \approx 13e^{-0.12u}$ s^{-1}, and $k_{43} \approx 20e^{0.12u}$ s^{-1}. The prominent effects of k_{21} on the temporal responses and of k_{12} on their amplitudes have already been mentioned above (Fig. 4 *B*; Fig. 5, *E* and *F*). Maximum turnover of the system at large V-displacements from equilibrium is given by k_{34} (for import) and k_{43} (for export) because these rate constants for reorientation of the empty binding site have a weaker V-sensitivity ($z_E = -0.3$) than the corresponding ones (k_{12} and k_{21}) for the occupied binding site ($z_C = 0.7$).

The impact of $k_{21}^0 k_{43}^0/(k_{12}^0 k_{34}^0) \approx 25$ on the preferential opening of the cavity of MSF transporters to inside has already been pointed out.

The reference stability constant of $K_1^0 \approx 3\mu M^{-3}$ corresponds to an inner K_D of $1/K_1 \approx 0.3$ μM nitrate at $pH_i = 6$. This means that at physiological $pH_i = 7.4$ the internal complex is very unstable confirming a low pK_a of Glu^{325} in this state (7), and facilitating the unloading of the complex. With the known parameters K_1^0, k_{12}^0, k_{21}^0, k_{34}^0, k_{43}^0, Eq. 3c yields an $K_2^0 \approx 0.3\,\mu M^{-3}$ corresponding to an external K_D of $1/K_2 \approx 3$ μM nitrate at $pH_o = 6$.

c_{i0}, c_{i1}

The internal substrate concentrations, c_{i0} and c_{i1} in the absence and presence of external NO_3^-—which are actually product concentrations if the transporter is viewed as an enzyme that catalyzes nitrate uptake—are treated here as internal NO_3^- concentrations as if the concentration of the cosubstrate $[H^+]_i$ were constant. In reality, the internal substrate concentration of the symporter is $c_i = [H^+]_i^2 \times [NO_3^-]_i$ in mM^3 or μM^3. In other words, the listed changes from c_{i0} to c_{i1} in Table 1 are only $[NO_3^-]_i$ changes in part because of parallel and probably bigger changes in $[H^+]_i^2$.

This precautious remark on c_i refers to local and temporal conditions in the close vicinity of the membrane. It does not apply for c_o because $[H^+]_o$ is kept constant by the experimenter.

Alternative interpretation?

It has been mentioned that the nitrate induced $\Delta I(V, t)$ recorded with fast V-protocols, has similarities with capacitive currents. So one may ask whether the observed phenomenon is, in fact, not due to the kinetics of the enzymatic cycle but due to a nitrate-induced increase of the membrane capacity itself, e.g., due to nitrate-induced fusion of cytoplasmic vesicles with the plasma membrane. In this case, the vertical displacement between $\Delta I(V, t)$ for positive and negative $\Delta V/\Delta t$, should be insensitive to V, because the membrane capacitance is basically V-independent. This possibility has to be rejected because in the recordings to Fig. 3, *B–D*, this displacement increases with positive going V, which indicates the effect of a very nonlinear device, i.e., exactly the proposed reaction cycle (Fig. 1 *B*) with its V-sensitive rate constants (Eqs. 1a–1d), as demonstrated by the good fits.

CONCLUSIONS

1. Fast, triangular V-protocols enable detailed electrophysiological investigations over a wider V-range than conventional step/steady-state V-protocols.
2. Corresponding experimental data are adequate to determine all 11 parameters of a general, reaction kinetic model for nonlinear electrodynamics of ion translocation.
3. The method allows identification of the physical function of ion transporters in considerable detail.
4. The kinetic characteristics of EnNRT determined here are suitable to quantify mechanistic models of MSF transporters.

We thank Jim (J. R.) Kinghorn (University of St. Andrews, Scotland) for the DNA of EnNtr.

This work has been supported by grants from the Natural Sciences and Engineering Research Council of Canada (to CMB).

REFERENCES

1. Zagotta, W. N., T. Hoshi, and R. W. Aldrich. 1994. Shaker potassium channel gating. III. Evaluation of kinetic models for activation. *J. Gen. Physiol.* 103:321–362.
2. Zei, P. C., and R. W. Aldrich. 1998. Voltage-dependent gating of single wild-type and S4 mutant KAT1 inward rectifier potassium channels. *J. Gen. Physiol.* 112:679–713.
3. Neher, E., and C. F. Stevens. 1977. Conductance fluctuations and ionic pores in membranes. *Annu. Rev. Biophys. Bioeng.* 6:345–381.
4. Läuger, P. 1980. Kinetic properties of ion carriers and channels. *J. Membr. Biol.* 57:163–178.
5. Läuger, P. 1995. Conformational transitions of ionic channels. *In* Single-Channel Recording, 2nd Ed. B. Sakmann and E. Neher, editors. Plenum, New York, NY. 651–662.
6. Beilby, M. J., and N. A. Walker. 1981. Chloride transport in *Chara* I. Kinetics and current-voltage curves for probable proton symport. *J. Exp. Bot.* 32:43–54.
7. Abramson, J., I. Smirnova, V. Kasho, G. Verner, H. R. Kaback, and S. Iwata. 2003. Structure and mechanism of the lactose permease of *Escherichia coli*. *Science*. 301:610–615.
8. Unkles, S., K. L. Hawker, C. Grieve, E. Campbell, and J. R. Kinghorn. 1991. crnA encodes a nitrate transporter in *Aspergillus nidulans*. *Proc. Natl. Acad. Sci. USA*. 88:204–208.
9. Boyd, J., D. Gradmann, and C. M. Boyd. 2003. Transinhibition and voltage-gating in a fungal nitrate transporter. *J. Membr. Biol.* 195: 109–120.
10. Lanyi, J. K., and B. Schobert. 2003. Mechanism of proton transport in bacteriorhodopsin from crystallographic structures of the K, L, M1, M2, and M2′ intermediates of the photocycle. *J. Mol. Biol.* 328:439–450.
11. Hansen, U. P., D. Gradmann, D. Sanders, and C. L. Slayman. 1981. Interpretation of current-voltage relationships for ''active'' ion trans-

port systems. I. Steady-state reaction-kinetic analysis of class-I mechanisms. *J. Membr. Biol.* 63:165–190.

12. Gradmann, D., U. P. Hansen, and C. L. Slayman. 1982. Reaction kinetic analysis of current-voltage relationships for electrogenic ion pumps in *Neurospora* and *Acetabularia*. *Curr. Top. Membr. Transp.* 16:257–276.
13. Rakowski, R. F., and C. L. Paxson. 1988. Voltage dependence of Na/K pump current in *Xenopus* oocytes. *J. Membr. Biol.* 106:173–182.
14. Gradmann, D., and C. M. Boyd. 2000. Three types of membrane excitations in the marine diatom *Coscinodiscus wailesii*. *J. Membr. Biol.* 175:149–160.
15. De Weer, P., D. C. Gadsby, and R. F. Rakowski. 2001. Voltage dependence of the apparent affinity for external Na(+) of the backward-running sodium pump. *J. Gen. Physiol.* 117:315–328.
16. Tittor, J., U. P. Hansen, and D. Gradmann. 1983. Impedance of the electrogenic Cl^- pump in *Acetabularia*: electrical frequency entrainments, voltage-sensitivity and reaction kinetic interpretation. *J. Membr. Biol.* 75:129–139.
17. Rakowski, R. F. 1993. Charge movement by the Na/K pump in Xenopus oocytes. *J. Gen. Physiol.* 101:117–144.
18. Allen, G. J., D. Sanders, and D. Gradmann. 1998. Calcium-potassium selectivity: kinetic analysis of current-voltage relationships of the open, slowly activating channel in the vacuolar membrane of guard-cells of *Vicia faba*. *Planta*. 204:528–541.
19. Stühmer, W. 1992. Electrophysiological recording from *Xenopus* oocytes. *Methods Enzymol.* 207:319–339.
20. Zhou, J. J., L. J. Trueman, K. J. Boorer, F. L. Theodoulou, B. G. Forde, and A. J. Miller. 2000. A high affinity fungal nitrate carrier with two transport mechanisms. *J. Biol. Chem.* 275:39894–39899.
21. Gradmann, D., and C. M. Boyd. 1999. Electrophysiology of the marine diatom *Coscinodiscus wailesii*. IV. Types of non-linear current-voltage-time relationships recorded with single saw-tooth voltage-clamp. *Eur. Biophys. J.* 28:591–599.
22. Gradmann, D., and C. M. Boyd. 2004. Current-voltage-time records of ion translocating enzymes. *Eur. Biophys. J.* 33:396–411.
23. Gradmann, D., and C. M. Boyd. 2005. Apparent charge of binding site in ion translocating enzymes: kinetic impact. *Eur. Biophys. J.* n press.
24. Kocic, I., Y. Hirano, and M. Hiraoka. 2004. The effects of K^+ channels modulators terikalant and glibenclamide on membrane potential changes induced by hypotonic challenge of guinea pig ventricular myocytes. *J. Pharmacol. Sci.* 95:27–32.
25. Fohlmeister, J. F., and W. J. Adelman, Jr. 1987. Gating current harmonics. IV. Dynamic properties of secondary activation kinetics in sodium channel gating. *Biophys. J.* 51:335–338.
26. Huang, Y., M. J. Lemieux, J. Song, M. Auer, and D. N. Wang. 2003. Structure and mechanism of the glycerol-3-phosphate transporter from Escherichia coli. *Science*. 301:606–620.
27. Sagar, A., and R. F. Rakowski. 1994. Access channel model for the voltage dependence of the forward-running Na+/K+ pump. *J. Gen. Physiol.* 103:869–893.
28. Hansen, U. P., J. Tittor, and D. Gradmann. 1983. Interpretation of current-voltage relationships for ''active'' ion transport systems. II. Non-steady-state reaction-kinetic analysis of class-I mechanisms. *J. Membr. Biol.* 75:141–169.
29. Hookes, R., and T. Jeeves. 1961. Direct search solution of numerical and statistical problems. *J. Assoc. Comput. Mach.* 8:212–229.
30. Schmitt, B. M., and H. Koepsell. 2002. An improved method for real-time monitoring of membrane capacitance in *Xenopus laevis* oocytes. *Biophys. J.* 82:1345–1355.
31. Solsona, C., B. Innocenti, and J. M. Fernandez. 1998. Regulation of exocytotic fusion by cell inflation. *Biophys. J.* 74:1061–1073.
32. Zampighi, G. A., M. Kreman, K. J. Boorer, D. D. Loo, F. Bezanilla, G. Chaudry, J. E. Hall, and E. M. Wright. 1995. A method for determining the unitary functional capacity of cloned channels and transporters expressed in *Xenopus laevis* oocytes. *J. Membr. Biol.* 148:66–78.
33. Morais-Cabral, J., Y. Zhou, and R. MacKinnon. 2001. Energetic optimization of ion conduction rate by the K^+ selectivity filter. *Nature*. 414:37–42.
34. Bernèche, S., and B. Roux. 2001. Energetics of ion conduction through the K^+ channel. *Nature*. 414:73–76.